



© WIKIPEDIA

BY MINGZHU LU,
XIAODONG WANG,
MINGXI WAN, YI FENG,
FENG XU, HUI ZHONG,
AND JINWEN TAN

High-intensity focused ultrasound (HIFU) has been testified as a promising surgical modality to ablate deep-seated tumors noninvasively and precisely [1]–[4]. The faster pace of the advanced HIFU technology owes a great deal to the sufficiently sophisticated imaging techniques and the significant advancements in high-power ultrasound transducers, which now allow the focused ultrasound surgery system to be more reliable and precise [1]–[7]. The early pioneer work in the clinical trials and HIFU clinical equipment carried out by the researchers in China (Chongqing, Beijing, and Shanghai) are valuable and encouraging in the world of HIFU [8]. The ultrasound-guided equipment of the JC HIFU system has been put into clinical trials, both in China and Oxford, United Kingdom [9]. Now, a variety of tumors such as those in the liver, breast, kidney, and pancreas as well as the uterine fibroids and osteosarcoma are treated clinically with focused ultrasound surgery [8]–[12].

Currently, either diagnostic ultrasound or magnetic resonance imaging (MRI) has been used for image guidance in focused ultrasound surgery. The MRI guidance has the advantages of better image quality and the ability to monitor temperature, but the price of the MRI-compatible system is relatively high. Nevertheless, ultrasound guidance has the remarkable merits of cheaper cost as well as the capability of a near-real-time image monitor.

Typically, there are two types of therapeutic transducers: one is a single-element applicator and the other is a phased array. The phased array offers several advantages over the single-focused transducers, such as electronically steering foci in three-dimensional (3-D) spaces, providing subarray modalities to avoid the beam obstacles like human rib cages, and correcting the beam distortions caused by the focused beam through the human skull and tissue inhomogeneity [12]–[16]. To correct the distortions arising from transmission through the skull bone, large apertures with hundreds of phased arrays were employed [7], [13], [14].

Previously, we developed a number of algorithms and methods that are basically important for the precise multifocus control in the phased-array focused ultrasound surgery, such as the explicit expression of the spherical-section phased-array pressure calculation [15], the genetic algorithm for multifocus pattern opti-

Image-Guided 256-Element Phased-Array Focused Ultrasound Surgery

System and Multifocus Pattern Control

mal control [15], and the subarray modalities to steer the beam avoiding the human rib-cage obstacles in noninvasive surgery [16].

In this article, we first describe the construction and functions of our ultrasound-guided 256-element phased-array surgery system. We then concentrate on several flexible multifocus control methods for accurate, highly efficient, and fit-to-shape ultrasound surgery. Then, the simulation and experiment results are implemented to support the multifocus control methods.

Image-Guided 256-Element Phased-Array Ultrasound Surgery System

System Description

Figure 1 shows the state of the art of our image-guided 256-element phased-array ultrasound surgery system. The system employs an extracorporeal therapy transducer, a 256-element phased-array applicator, for noninvasive focused ultrasound surgery. A diagnostic ultrasound device is introduced in the system for image guidance in surgery. The therapeutic phased arrays combined with the diagnostic probe are mounted in a water bag of degassed water, below the center of the therapeutic bed. The ultrasound is directed upward, and the degassed water provides acoustic coupling between the transducer and the patient. The integration of the therapeutic transducer and the image probe mounted on the 3-D robotic positioner can move in 3-D to target and identify tumors precisely. The surgeon can perform the ultrasound surgery conveniently on the current diagnostic image in the main control computer through the surgery procedures of 3-D navigation, targeting, and monitoring. The main control computer with the main operative program controls the main subsystems: the 256-channel phased-array driving system that drives the 256-element phased array, the robotic electrical controller that controls the 3-D robotic positioner's movement, the image acquisition that acquires the image from the diagnostic ultrasound image system, and the degassed water device.

256-Element Phased Array and 256-Channel Driving System

The 256-element spherical-section phased array, which is designed by us (see Figure 2), is constructed from 1-3 piezocomposite material and operates at a frequency of 1.1 MHz. The array has a 14-cm outer diameter, with a 3.4-cm diameter central hole

Digital Object Identifier 10.1109/MEMB.2008.923952

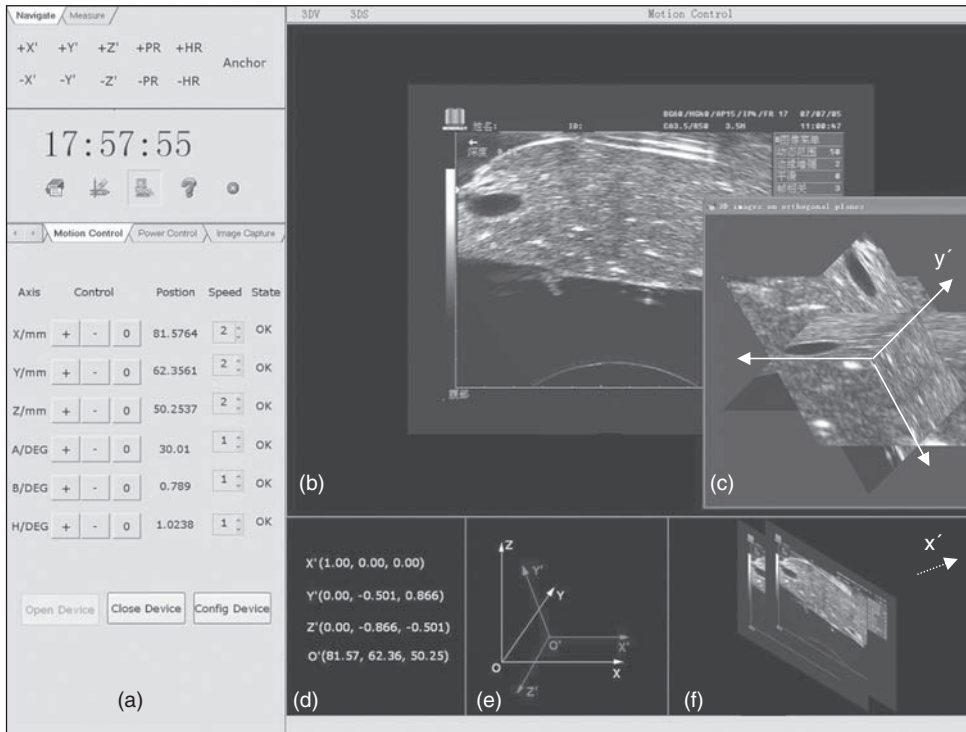


Fig. 3. The navigation submenu interface of the image-guided main operative program.

are used for the current ultrasound image [see Figure 3(e)]. Two methods take important part in the realization of viewpoint-based navigation. One is the parallel control of the six axis movements, and the other is the calculation algorithms in the operative program, where based on the established two coordinate systems and developed two coordinate transform matrixes, the six axial displacements are calculated automatically from the viewpoint-based 3-D navigation data.

Figure 3 shows the navigation submenu interface of the main operative program for 3-D navigation. The current ultrasound image displays the main image window [Figure 3(b)], on which a surgeon can perform viewpoint-based 3-D navigation. The submenu functions of the six axis movements and viewpoint-based 3-D displacements are shown in Figure 3(a). The volumes of data may be acquired from the scan image along one direction [see Figure 3(f)]. Figure 3(c) shows the pop-up image window of 3-D images on orthogonal planes. Figure 3(c) and (f) provide a surgeon with 3-D structural orientation within the target organ. The left window [Figure 3(a)] in the interface of the main operative program can be changed to other submenu functions like therapy planning.

The system obtains the multimodality 2-D or 3-D images in a digital imaging and communications in medicine (DICOM) format file from computed tomography (CT), MRI, and positron emission tomography (PET). The multimodality image registration is based on a point-based registration in which the operator identifies the parenchymal organ's landmarks in the image obtained from DICOM file and current diagnostic image. The least-square fitting algorithm is applied to correct the point-matching registration, and the coordinate transformations can be established. To acquire the high-quality and real-time volume rendering, a Volume Pro 1000 card is used.

The therapy planning on the ultrasound image of a slice can be implemented by drawing the outline of the therapy region and by

setting the focus patterns and other therapy parameters. A lesion is formed by a sonication with a focus pattern; a linear lesion is formed by a set of sonications in succession. The region therapy is composed of those linear lesions. The sonication priority for therapy is first the farthest region and last the nearest region. The transient monitoring image includes the gray image and the transient lesion image, based on digital technique sum squared differences that are acquired from radio frequency data frames [17].

Multifocus Pattern Control

Accurate Field Calculation

A spherical-section phased array shown in Figure 2 has the same rectangular projection area ΔA . The width

and height of each element projection are Δw and Δh , respectively. Previously, an efficient field-calculation formula of the explicit expression [15] that comes from Rayleigh-Sommerfeld integral was developed. In our further research, we improved the previous explicit expression for spherical-section phased array, which is

$$p = \frac{j\rho ck}{2\pi} \sum_{n=1}^N u_n \frac{F_n \Delta A}{R_n} e^{-(\alpha+jk)R_n} \sin c \frac{kx_{sn}\Delta w}{2R} \sin c \frac{ky_{sn}\Delta h}{2R}, \quad (1)$$

where p is the complex acoustic pressure at a point, $j = \sqrt{-1}$, ρ and c are the density (kg/m^3) and sound speed (m/s) in medium, respectively, $k = \omega/c$ is the wavenumber, N is the number of element, α is the sound attenuation coefficient [$\text{Np}/(\text{m MHz})$], u_n is the particle velocity (m/s) of n th array element. Other parameters are calculated as

$$R_n = \sqrt{(z - z_n)^2 + (y - y_n)^2 + (x - x_n)^2}, \quad (2)$$

$$F_n = \frac{R_{SR}}{\sqrt{R_{SR}^2 - (x_n^2 + y_n^2)}}, \quad \text{and} \quad R_{zn}^2 = R_{SR}^2 - (x_n^2 + y_n^2), \quad (3)$$

$$x_{sn} = x + \frac{z - R_{SR}}{R_{zn}} x_n, \quad \text{and} \quad y_{sn} = y + \frac{z - R_{SR}}{R_{zn}} y_n. \quad (4)$$

The accurate explicit expression (1) is nearly the same as the previous expression; the only difference between the two is the distance R_n appearing in the exponential term of (1) instead of R_{sn} in the previous expression. In the derivation of previous expression, the distance r in the exponential term of Rayleigh-Sommerfeld integral has the square root form with respect to parameters, such as x or y . To make the exponential term integrable, we previously used the strategy of the

The MRI guidance has the advantages of better image quality and the ability to monitor temperature.

binominal expansion of this distance r . Nevertheless, in this step of the binominal expression, we kept only the first two terms and omitted the other high-order nonlinear terms. This omitting may bring an error in certain circumstances, such as large-aperture phased arrays. To compensate this error, a more accurate expression (1) is formed here. The details to testify the accuracy of the expression (1) will be presented in another article.

Fit-to-Shape Multifocus Patterns

The combined method made up of the accurate explicit expression (1) and the genetic algorithm [15] is used to obtain a set of array driving signals corresponding to a focus pattern. Each set of driving signals is put into the focus pattern library for later ultrasound surgery use. The focus pattern library consists of all the possible focus patterns; thus, a set of driving signals correlated with a focus pattern can be promptly selected from the focus pattern library in the course of ultrasound surgery.

The more the number of elements the array has, the more flexible or the more complex-shaped multiple foci can be

formed. We can use the fit-to-shape multifocus pattern to target the tissue surrounded by important tissue. Normally, the fit-to-shape multifocus pattern can be arranged in the shapes of S, X, O, square, etc. The criteria for the design of the fit-to-shape multifocus patterns are as follows:

- 1) The number of array elements should be four times more than the number of foci of fit-to-shape multifocus pattern.
- 2) The peak intensity at each focus should be larger than $1,000 \text{ W/cm}^2$.
- 3) The multifocus locations that do not overlay are ranged to have low level of side lobes.

Random Signal Control

By using the combined method, a variety of simulations can be implemented for analysis of many actual focus circumstances, such as to mimic the practical array-driving control system with random system control error by means of adding additional random signals to the normal array-driving signals. The situations of both single focus and multiple foci influenced by using the additional random-amplitude signals and

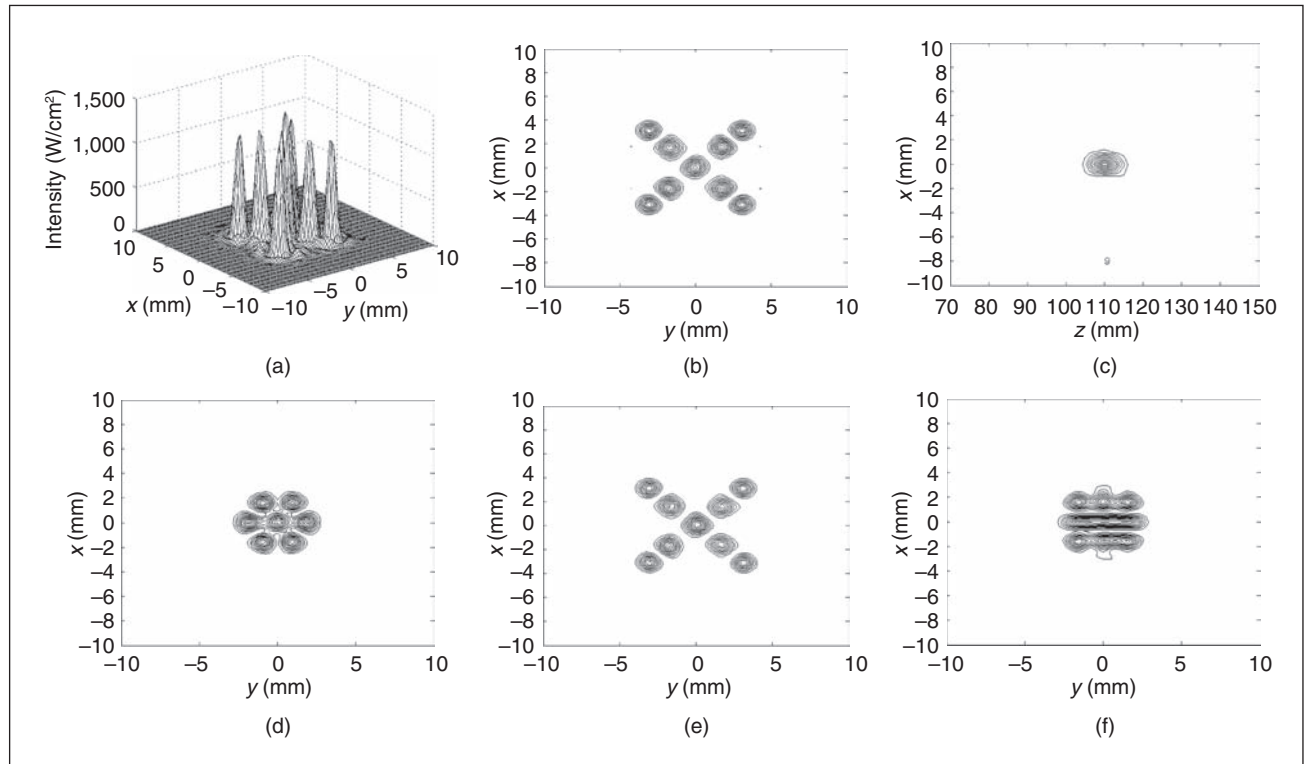


Fig. 4. The fit-to-shape multifocus pattern of nine foci in X shape. (a) The intensity profile at focus plane. (b) x-y contour plot. (c) x-z contour plot of X. x-y contour plots of fit-to-shape multifocus patterns: (d) Q-shaped focus pattern. (e) X-shaped focus pattern with additional 30% main-max random-amplitude driving signal. (f) Square-shaped focus pattern with nine foci and with the additional 20% main-max random-phase driving signal.

additional random-phase signals to the normal array-driving signals have been analyzed systematically and can be summed up as follows. Generally, the focus positions are unmoved when using the additional random amplitude signals, larger or small, while peak intensity may lower a little bit; the focus positions depend on the accurate phase signal control, and the multifocus pattern needs more accurate phase signal control than the single focus condition. As a result, the system can assure the designed focus positions and peak intensities when the additional random amplitude and phase signals are less than 10% of the main-max driving signals.

Ideally, the therapy demands a sharply focused intensity distribution at the focus without grating lobes and with low level of the side lobes. In addition, the therapy demands the target tissue temperature be 56 °C more than the tissue-protein denature temperature without cold spots inside the focal region of multiple foci. To arrive at these two goals or to improve the therapeutic properties, we adopt three schemes of random control. The additional random-amplitude signals on original control may not influence the focus positions but can have the effect of reducing the levels of the side lobes. The first random control method is that the larger than 10% main-max random-amplitude signals will be added purposely to the original amplitude driving signals. As a result, the additional random-amplitude signal condition

will bring the effect of suppressing unwanted grating lobes and side lobes. Additional random phase signals that are too large may change the focus positions, but a certain amount of additional random-phase signals may have the effect of increasing the levels of the side lobes. The second random control method is to add additional random-phase signals to the original phase-driving signals. The additional random-phase signals have the effect of elevating the intensity valley by increasing side lobe levels inside the region of multiple foci, thus fuzzing the tightly arranged multiple foci to obtain the therapeutic result of no cold spots inside the focal region of multiple foci. The third random control method is to randomly arrange the multifocus locations within a certain range to fuzz the multiple foci.

Results

The transducer was used in the simulation above the 256-element phased array. Normal exciting signals were obtained by using the combined method in the simulation. In the simulation, the homogeneous loss medium density ρ , sound speed c , and water attenuation coefficient α were 1,000 kg/m³, 1,500 m/s, and 0.000115 Np/(cm · MHz), respectively.

Figure 4(a)–(f) shows the simulations of the fit-to-shape multifocus patterns. Three styles of the intensity profiles of X-shaped display are shown in Figure 4(a)–(c). The peak intensity at focus is larger than 1,000 W/cm² in Figure 4(a), and each single focus has the size of 1.25 mm × 1.25 mm × 9 mm. If you look carefully at the focus distribution in Figure 4(b), you will find beside the foci three small dots that are the side lobes of the level higher than -20 dB and less than -13.9 dB. Figure 4(d) shows the ideal large focus formed by multiple foci without cold spots inside the large focal region when making a lesion in the target tissue. We use three random control methods to improve focal properties, to reduce the level of side lobes, and to get thermally even lesions inside the large focus. To reduce the level of the side lobes, we use additional 30% main-max random-amplitude driving signals, and the effective result is shown in Figure 4(e), which shows no side lobes (no dots, which means the side lobe's level is below -20 dB in Figure 4(e), whereas Figure 4(b) shows three small dots). To get an even thermal lesion inside a large focus, we use two random control methods. As a control result of the additional 20% main-max random-phase driving signals,

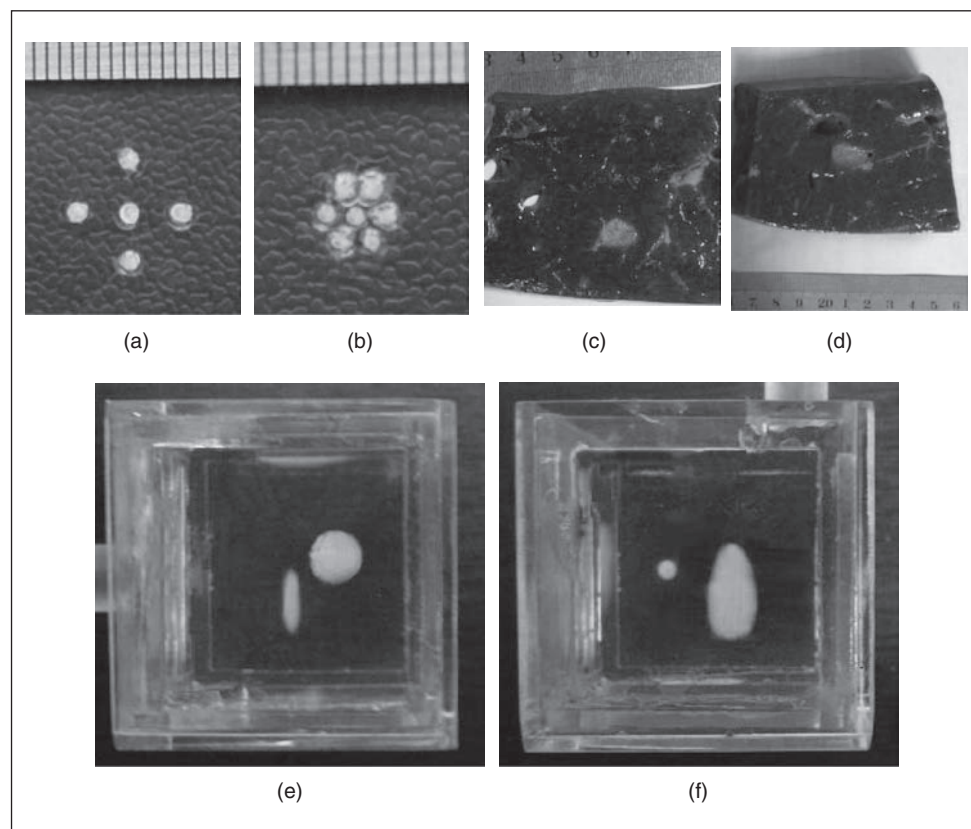


Fig. 5. (a) The marks of five single foci are formed on a transparent, thin slice of polymethyl methacrylate. The center, left, right, up, and down marks are the on axial foci of (0, 0, 108) mm, off axial foci of (-4, 0, 108) mm, (4, 0, 108) mm, (0, 4, 108) mm, and (0, -4, 108) mm, respectively. (b) The marks of a Q-shaped multifocus pattern are formed on a transparent, thin slice of polymethyl methacrylate. Cross section of bovine liver after exposures: (c) A lesion with Q-shaped multifocus pattern. (d) A lesion with single focus moving at a speed of 0.8 mm/s. (e) Visualization of lesions of a single-focus pattern and the Q-shaped multifocus pattern (the larger lesion) in a transparent tissue-mimicking phantom with BSA. (f) Side view of (e).

Table 1. Experiment results in the BSA tissue-mimicking phantom and bovine liver in Figure 5.

Material	Focus Patterns in Figure 5(c)–(f)	Total Acoustic Power (W) and Sonication Time (s)	Lesion Dimensions $x_M \times y_M \times z_M$ (mm ³)
BSA phantom	Single focus in Figure 5(e) and (f)	109 (25)	2.2 × 2.2 × 9
	Q-type multifoci in Figure 5(e) and (f)	84 (25)	5.3 × 5.3 × 11
Bovine liver	Q-type multifoci in Figure 5(c)	222 (3)	10 × 10 × 9
	Linear moving of single focus in Figure 5(d)	122 (20)	20 × 3 × 9

Figure 4(f) shows the fuzzed focal region of the square-shaped large focus composed of nine foci. To get the effect of a fuzzed focal region, we can use the control method of randomly arranging the multifocus locations within the focal region.

Figure 5 shows the experiment results of our surgery system. A transparent, thin slice of polymethyl methacrylate with 1–2-mm thickness is placed at the position of the focus plane; marks will be made at exact focus positions on the slice when short and high-intensity ultrasound emit. Five single focuses are formed, respectively, on the thin slice in Figure 5(a), with 50-W total acoustic power (for each single focus) applied to the transducer (the electroacoustic efficiency is 70%; therefore, 71 W of electrical power is needed) and 1-s sonication time. Q-shaped multiple foci [same pattern as Figure 4(d)] are formed on the thin slice in Figure 5(b), with 50-W total acoustic power and 1-s sonication time. The results of the focus marks in Figure 5(a) and (b) indicate that the focus positions are exactly at designed locations, and the experiment results agreed well with the simulations.

An optically transparent polyacrylamide gel (40 mm × 40 mm × 40 mm) containing bovine serum albumin (BSA) [19] was used in experiments as a tissue-mimicking phantom. The density, sound speed, attenuation coefficient, specific heat, and thermal conductive of the BSA tissue-mimicking phantom were 1,060 kg/m³, 1,600 m/s, 0.07 Np/(cm · MHz), 3,850 J/(kg · K), and 0.55 W/(cm · K), respectively. The white lesion that indicates that the BSA protein became thermally denatured will form at the focus place in the transparent phantom shortly after HIFU sonication. Figure 5(e) and (f) shows two lesions, one small and one big. The small lesion was formed by the single focus, with 109-W total acoustic power and 25 s sonication time. The big lesion was formed by the Q-shaped multifocus pattern [same patterns as Figure 4(d)] with 84-W total acoustic power and 25-s sonication time. The volume of the big lesion is 6.6 times larger than that of the small lesion. Therefore, using the Q-shaped multifocus pattern will shorten the therapy time greatly.

Two experiment results of bovine liver are shown in Figure 5(c) and (d). Figure 5(c) shows a large lesion formed inside the bovine liver, which is of 10 mm × 10 mm × 9 mm, using multifocus Q-shaped pattern control, total acoustic power of 222 W, and 3-s sonication time. Figure 5(d) shows a large linear-shaped lesion formed inside the bovine liver, which is of 20 mm × 3 mm × 9 mm, using single focus moving at a speed of 0.8 mm/s, 16-mm linear distance, and total acoustic power of 122 W. Table 1 contains a summary of lesions formed in BSA phantom and in bovine liver shown in Figure 5(c)–(f).

Discussion

A series of simulations testify that many fit-to-shape multifocus patterns have excellent field properties and can be applied to

focused ultrasound surgery. Different random control methods have different effects on multifocus patterns. The less than 5% main-max random signals do not have any effect on the original properties of multiple foci at all. The additional random-amplitude driving signals, larger than 10% main-max, may reduce the level of the side lobes (same effect as the sparse random-phased array [18]). The additional random-phase driving signals and randomly arranging the multifocus locations within the focal region may help to make the lesion thermally even.

The experiment results confirm that the system can control complex focus patterns precisely. The focus positions and shapes of the experiments agreed well with the simulations. With the same ultrasound exposure dosage, the large lesion volume is 6.6 times larger than that of the single focus.

In our experiments of single-focus patterns, when less than 100 W of the total acoustic power is employed and the lesion is formed at a depth of 2–3 cm in bovine liver tissue or in the tissue-mimicking phantom, the lesion has a cigar-like shape. When more than 130 W of total acoustic power is employed and the lesion is formed at a depth of 2–3 cm in bovine liver tissue or in the tissue-mimicking phantom, the lesion has a tadpole-like shape and moves toward the transducer, which means the cavitation may contribute more to the lesion shape in the situation [19].

The fit-to-shape focus patterns may be classified into two types. One has the shape of X, S, C, etc., which is suitable to the target tissue surrounded by the important tissue like the important nerve or blood vascular. Another type has the large focal shapes such as square and Q shapes, which has the excellent therapeutic property of an even thermal large lesion. The square-shaped multifocus pattern may be more welcome in making linear or cubic lesions with multiple sonications, because the smallest focal zone overlay between two successive sonications is needed in this type of focus pattern, and the lesion edges may appear smooth.

Summary

An image-guided phase array therapy system has been developed. In this article, we have presented the comprehensive system functions and framework, as well as the multifocus pattern control methods. The system experiment results show that the multiple foci are positioned exactly at designed locations. In addition, the experiment results agreed well with the simulations.

Acknowledgments

This project was supported by the National Natural Science Foundation of China under Grant Nos. 30630024 and 10674108.

Mingzhu Lu received her B.S. degree from the Department of Scientific Instrumentation, Zhejiang University, in 1982, and the M.S. and Ph.D. degrees in automatization and in biomedical engineering from Xi'an Jiaotong University in 1990 and 2004,



respectively. She works as a professor in the Department of Biomedical Engineering in Xi'an Jiaotong University, where she is pursuing the development of a HIFU system. Her research interests are applications of ultrasound, particularly HIFU for noninvasive surgery and modeling in biomedical system.



Xiaodong Wang received his B.S. and M. S. degrees, both in biomedical engineering, from Xi'an Jiaotong University in 1997 and 2000, respectively. He is currently pursuing a Ph.D. degree in biomedical engineering at Xi'an Jiaotong University. His research interests include medical instrumentation and application system of HIFU for noninvasive surgery.



Mingxi Wan received his B.S. degree in geophysical prospecting in 1982 from Jiangnan Petroleum Institute, and the M.S. and Ph.D. degrees in biomedical engineering from Xi'an Jiaotong University in 1985 and 1989, respectively. Now, he is a professor and chair of the School of Life Science and Technology of Xi'an Jiaotong University. He was a visiting scholar and adjunct professor at Drexel University and the Pennsylvania State University from 1995 to 1996 and a visiting scholar at University of California, Davis, from 2001 to 2002. He has authored and coauthored more than 100 publications and three books about medical ultrasound. He is a recipient of several important awards of the Chinese government and universities. His current research interests are medical ultrasound imaging, especially tissue elasticity imaging, contrast and tissue perfusion evaluation, HIFU, and voice science. He is a Member of the IEEE.



Yi Feng received a bachelor's degree from Xi'an Jiaotong University in 2002. She is currently pursuing a Ph.D. degree in biomedical engineering at Xi'an Jiaotong University. Her research interests include the biological processes related to biomedical ultrasound as well as the preparation of the polyacrylamide-based phantom for the research of therapeutic ultrasound.



Feng Xu received his B.S. and M.S. degrees from Northwestern Polytechnical University in 1998 and 2001, respectively. He is currently working toward a Ph.D. degree in biomedical engineering at Xi'an Jiaotong University. His research interests are beam forming and the application of HIFU.



Hui Zhong received her B.S. and Ph.D. degrees in biomedical engineering from Xi'an Jiaotong University in 2000 and 2006, respectively. She is currently an instructor in the Department of Biomedical Engineering at Xi'an Jiaotong University. Her research interests are medical ultrasound imaging and its application for HIFU.



Jinwen Tan received his B.S. degree in biomedical engineering from Xi'an Jiaotong University in 2006. He is currently pursuing an M.S. degree in biomedical engineering at Xi'an Jiaotong University. His research interest is the development of software for a HIFU application system.

Address for Correspondence: Mingxi Wan, The Key Laboratory of Biomedical Information Engineering of Ministry of Education, Xi'an Jiaotong University, Xi' an 710049, China. E-mail: mxwan@mail.xjtu.edu.cn.

References

- [1] G. ter Haar, "Therapeutic applications of ultrasound," *Prog. Biophys. Mol. Biol.*, vol. 93, no. 1-3, pp. 111-129, 2007.
- [2] S. P. Dimaio, N. Archip, N. Hata, I. Talos, S. K. Warfield, A. Majumdar, N. Mcdannold, K. Hynynen, P. Morrin, W. Wells, D. Kacher, R. Ellis, A. Golby, F. Black, F. Jolesz, and R. Kikinis, "Image-guided neurosurgery at Brigham and Women's Hospital," *IEEE Eng. Med. Biol. Mag.*, vol. 25, no. 5, pp. 67-73, 2006.
- [3] J. L. Foley, S. Vaezy, and L. A. Crum, "Applications of high-intensity focused ultrasound in medicine: Spotlight on neurological applications," *Appl. Acoust.*, vol. 68, no. 3, pp. 245-259, 2007.
- [4] G. ter Haar, "Acoustic surgery," *Phys. Today*, vol. 54, no. 12, pp. 29-34, 2001.
- [5] G. T. Clement, "Perspectives in clinical uses of high-intensity focused ultrasound," *Ultrasonics*, vol. 42, no. 10, pp. 1087-1093, 2004.
- [6] K. Hynynen, G. T. Clement, N. Mcdannold, N. Vykhodtseva, R. King, P. J. White, S. Vitek, and F. A. Jolesz, "500-element ultrasound phased array system for noninvasive focal surgery of the brain: A preliminary rabbit study with ex vivo human skulls," *Magn. Reson. Med.*, vol. 52, no. 1, pp. 100-107, 2004.
- [7] D. R. Daum and K. Hynynen, "A 256-element ultrasonic phased array system for the treatment of large volumes of deep seated tissue," *IEEE Trans. Ultrason. Ferroelect. Freq. Contr.*, vol. 38, no. 7, pp. 634-644, 1999.
- [8] F. Wu, Z. Wang, W. Chen, W. Wei, G. Zhong, M. Zhang, G. Zheng, Y. Zhou, G. Xu, M. Li, C. Hang, H. Ye, and R. Feng, "Extracorporeal high intensity focused ultrasound ablation in the treatment of 1038 patients with solid carcinomas in china: An overview," *Ultrason. Sonochem.*, vol. 11, no. 3-4, pp. 149-154, 2004.
- [9] J. E. Kennedy, F. Wu, G. ter Haar, F. V. Gleeson, R. R. Phillips, M. R. Middleton, and D. Cranston, "High-intensity focused ultrasound for the treatment of liver tumors," *Ultrasonics*, vol. 42, no. 9, pp. 931-935, 2004.
- [10] F. Wu, Z. Wang, Y. Cao, Z. Xu, Q. Zhou, H. Zhu, and W. Chen, "Heat fixation of cancer cells ablated with high-intensity-focused ultrasound in patients with breast cancer," *Am. J. Surg.*, vol. 192, no. 2, pp. 179-184, 2006.
- [11] F. Wu, Z. Wang, H. Zhou, W. Chen, J. Zou, J. Bai, K. Li, C. Jin, F. Xie, and B. Su, "Feasibility of US-guided high-intensity focused ultrasound treatment," *Radiology*, vol. 236, no. 3, pp. 1034-1040, 2005.
- [12] H. L. Liu, N. Mcdannold, and K. Hynynen, "Focal beam distortion and treatment planning in abdominal focused ultrasound surgery," *Med. Phys.*, vol. 32, no. 5, pp. 1270-1280, 2005.
- [13] G. T. Clement and K. Hynynen, "A noninvasive method for focusing ultrasound through the human skull," *Phys. Med. Biol.*, vol. 47, no. 8, pp. 1219-1231, 2002.
- [14] M. Pernot, J. Aubry, M. Tanter, J. Thomas, and M. Fink, "High power transcranial beam steering for ultrasonic brain therapy," *Phys. Med. Biol.*, vol. 48, no. 12, pp. 2577-2589, 2003.
- [15] M. Lu, M. Wan, F. Xu, X. Wang, and H. Zhong, "Focused beam control for ultrasound surgery with spherical-section phased array: Sound field calculation and genetic optimization algorithm," *IEEE Trans. Ultrason. Ferroelect. Freq. Contr.*, vol. 52, no. 8, pp. 1270-1290, 2005.
- [16] X. Wang, M. Lu, and M. Wan, "Sub-array patterns of spherical-section phased array for high intensity focused ultrasound surgery," *Chin. J. Acoust.*, vol. 24, no. 1, pp. 10-20, 2004.
- [17] H. Zhong, M. Wan, Y. Jiang, and S. Wang, "Monitoring imaging of lesions induced by high intensity focused ultrasound based on differential ultrasonic attenuation and integrated backscatter estimation," *Ultrasound Med. Biol.*, vol. 33, no. 1, pp. 82-94, 2007.
- [18] S. A. Goss, L. A. Frizzell, J. Kouzmanoff, J. Barich, and J. M. Yang, "Sparse random ultrasound phased array for focal surgery," *IEEE Trans. Ultrason. Ferroelect. Freq. Contr.*, vol. 43, no. 6, pp. 1111-1121, 1996.
- [19] V. A. Khokhlya, M. R. Bailey, J. Reed, and L. A. Crum, "Effect acoustic nonlinearity propagation, cavitation, and boiling in lesion formation by high intensity focused ultrasound in a gel phantom," *J. Acoust. Soc. Am.*, vol. 119, no. 3, pp. 1834-1848, 2006.